J Paleolimnol (2017) 58:511–532
DOI 10.1007/s10933-017-0007-7

ORIGINAL PAPER

Geochemical imprints of coupled paleoenvironmental and provenance change in the lacustrine sequence of Orog Nuur, Gobi Desert of Mongolia

Kaifeng Yu · Frank Lehmkuhl · Bernhard Diekmann · Christian Zeeden · Veit Nottebaum · Georg Stauch

Received: 31 August 2016 / Accepted: 11 October 2017 / Published online: 17 October 2017

Abstract In the arid environment, due to the scarcity of a continuous terrestrial archive, lacustrine sequences are often employed as a paleoenvironmental repository. However, numerous spatial and temporal heterogeneities exist concerning previously studied sites in arid central Asia. Furthermore, surveys using a XRF core scanning technique on lacustrine sequences retrieved in hyperarid desert settings are largely rare. Hence, two parallel sediment cores (ONW I; ONW II) were retrieved from Orog Nuur, in the Gobi Desert of Mongolia. Continuous, high-resolution elemental abundances at a 1-cm scanning step size were examined in core ONW II using XRF core scanning. To constrain the data quality, elements with high error margins relative to measured peak areas and those elements/proxies below the significance level during the multivariate statistics are excluded for environmental/provenance implications. Based on multivariate statistical evaluation, the bulk-geochemistry of the core sediments are governed by (1) grain-size composition, (2) authigenic productivity (Ca, Cl, $CaCO_3$) in an alkaline environment, (3) allochthonous organic

---

Electronic supplementary material The online version of this article (doi:10.1007/s10933-017-0007-7) contains supplementary material, which is available to authorized users.

K. Yu (✉) · F. Lehmkuhl · C. Zeeden ·
V. Nottebaum · G. Stauch
Department of Geography, RWTH Aachen University,
Templergraben 55, 52056 Aachen, Germany
e-mail: kaifeng.yu@geo.rwth-aachen.de

F. Lehmkuhl
e-mail: flehmkuhl@geo.rwth-aachen.de

C. Zeeden
e-mail: c.zeeden@geo.rwth-aachen.de

V. Nottebaum
e-mail: veit.nottebaum@geo.rwth-aachen.de

G. Stauch
e-mail: georg.stauch@geo.rwth-aachen.de

B. Diekmann
Alfred Wegener Institute, Helmholtz Center for Polar and
Marine Research, Telegrafenberg A43, 14473 Potsdam,
Germany
e-mail: Bernhard.Diekmann@awi.de

K. Yu
Energy and Climate Change Division, Global Energy
Interconnection Development and Cooperation
Organization, 8 Inner Xuanwumen Str., Beijing 100031,
China

K. Yu
State Key Laboratory of Lake Science and Environment,
Nanjing Institute of Geography and Limnology, Chinese
Academy of Sciences, 73 East Beijing Rd.,
Nanjing 210008, China

material (TOC and C/N_{atomic}), and (4) terrigenous input via fluvial inflows, as well as quasi-constant aeolian input through the late Quaternary (Al, Si, K, Ti, and Fe). Disparate source lithotypes, as well as authigenic productivity of the lake system existed before and after Termination I. The Holocene was dominated by a distinct high productivity alkaline environment with more felsic and alkaline input relative to the late Pleistocene. This might be attributed to an increased hydrodynamic strength of riverine inflow and/or intensified erosion and weathering of felsic source rocks in the upper catchment of the Orog Nuur. Therefore, in order to gain a better understanding of the bulk-geochemistry of lake sediments, the coupled provenance and environmental signatures, as well as land surface processes in the catchment need to be systematically discerned. Thus, the XRF core scanning data obtained in this study would have practical and complimentary merit for other lacustrine studies focused on the desert realm across the globe.

Keywords XRF core scanning · Orog Nuur · Provenance · Grain size · Late Quaternary · Gobi Desert

Introduction

Lacustrine sequences are critical archives for the reconstruction of climate and provenance signatures. In particular, in arid central Asia, due to a scarcity of continuous loess-paleosol or oceanic archives, lacustrine records were often employed as Quaternary paleoenvironmental repositories (Boyle 2001; Mischke et al. 2005). Southern Mongolia is located on the margin of the westerlies-dominated arid central Asia and the East Asian Summer Monsoon domain of eastern Asia (Chen et al. 2008). Acquisition of a continuous and chronologically reliable past environmental record in this region is of substantial importance in refining our understanding of comprehensive paleoenvironmental patterns and possible driving mechanisms. However, numerous spatial and temporal heterogeneities exist concerning the lacustrine sequences here. Compared with more intensively studied lake records in northern China and northern Mongolia/Lake Baikal catchment of Russia, due to the remoteness of the region, only two continuous lacustrine records were previously reported in the Gobi Desert of Mongolia, namely Bayan Tohomin Nuur (nuur = lake; Felauer 2011) and Ulaan Nuur (Lee et al. 2011). Nonetheless, these two cores cover only the last ~ 15 ka. Furthermore, a commonly high reservoir effect (contributing to ^{14}C dating uncertainty) of the non-varved lacustrine sediments, as well as a lack of datable organic material in this arid context have largely hampered a robust age-depth reconstruction (Felauer 2011; Lee et al. 2011). A longer record along with a well constrained chronological model (for instance using Bayesian age-depth modelling) is therefore indispensable in providing a complementary repository to unravel the aforementioned issues.

Among a suite of multidisciplinary studies on argillaceous sediments, geochemistry appears to be a promising tool for deciphering the interplay between environmental change, source lithotypes and sediment bulk-composition (Boyle 2001). When considering late Quaternary lacustrine sediments, the bulk-geochemistry may be controlled by source terranes, authigenic or allogenic input, which may be modulated by past environmental conditions, while pedogenesis and diagenesis exert merely limited overprints (Yu et al. 2016). Knowledge of the downcore variability of major, trace, and minor element abundance along with field investigation and careful examination of previous geologic mapping will enable us to decipher the climate-induced provenance change throughout the depositional processes. On the other hand, surveys considering the bulk-geochemistry and corresponding environmental interpretations in the marine realm have been systematically reviewed (Calvert and Pedersen 2007), whilst elucidations of the elemental fingerprints incorporated in the lacustrine sediments still await more investigation (Roser and Korsch 1988; Norman and De Deckker 1990; Sinha et al. 2006). In particular, in contrast to conventional XRF measurement using pressed pellets, the application of high resolution, time saving, and continuous XRF core scanning to lake sediments has only attracted limited attention in the less than 10 years since its earlier applications in the marine realm (Melles et al. 2012). The XRF scanning technique has not yielded a complete consensus on how the provenance, depositional environment, and corresponding earth surface processes affect a suite of elements in different lacustrine settings (Richter et al.

2006; Shanahan et al. 2008). A recent review by Davies et al. (2015) highlights that several studies have been conducted to interpret elements, ratios and associated environmental interpretations in the lacustrine realm. However, those implications should not be taken as universally applicable, as there is to date rare XRF core scanning data that has been generated in the hyperarid (desert) setting where largely no varved laminae can be observed in the lacustrine sequences.

This work aims to provide a complementary XRF scanning logged record to fill in the gaps in the above mentioned spatial/temporal heterogeneity of data repositories in the hyperarid desert setting. In this study, major and trace element contents accompanied by calcium carbonate concentration and C/N_{atomic} ratios of the Orog Nuur lacustrine sequence are examined in an attempt to: (i) test the possible plots of element ratios that could be employed to extract the broad pattern of diversified source regions throughout the depositional period; and (ii) ultimately evaluate the set of multi-proxy fingerprints and parse out the interplay between the coupled past environmental processes, land surface processes, and provenance change in the arid depositional system of the Orog Nuur catchment.

Study area

The Orog Nuur (45°01′–45°04′N 100°33′–100°53′E; ~ 1219 m a.s.l.) is located in a hydrologically closed basin system in the Valley of Gobi Lakes (Fig. 1). It is a brackish lake subject to desiccation and occasionally turns into playa system. The Tuyn Gol (gol = river) is the main inflow originating from the southern slopes of the Khangai Mountains around 220 km north of the lake. The continental climate of Gobi Desert is characterized by a dry/cold winter with limited snow. More than 65% of the rainfall occurs in the summer. Annual precipitation reaches ~ 100 mm in the vicinity of the Orog Nuur in the Gobi Desert of Mongolia, while the higher elevated Khangai Mountains receive up to ~ 400 mm/a. The mean annual air temperature is − 2 to 5 °C. The mean air temperatures during July and January in the Gobi Desert are ~ 16 and ~ − 20 °C, respectively (Felauer 2011). The Valley of Gobi Lakes (1400–1800 m a.s.l.) is an elongated intramontane depression between the Siberian Craton and the Tarim and Sino-Korean Cratons (Baljinnyam et al. 1993; Cunningham 2005). Paleozoic volcanic and plutonic rocks are exposed in the basin (Fig. 1). The southern part of the Orog Nuur watershed is represented by the tectonic escarpment of the Gobi Altai, as well as gently inclined alluvial fans (Baljinnyam et al. 1993). As illustrated in Fig. 1, the northern catchment (Tuyn Gol watershed) is dominated with Devonian–Triassic felsic quartz syenite, granite, plagiogranite, and alkaline sediments, accompanied by minor proportions of (intermediate) mafic rocks. The southern watershed exhibits more mafic to ultramafic basalt and andesite-basalt rocks relative to the northern catchment. The Orog Nuur might have occupied a much larger area in the Eemian and Marine Isotope Stage 3 (Lehmkuhl and Lang 2001).

Materials and methods

Core retrieval and Bayesian age-depth modelling

During the playa phase in 2007 and 2008, two parallel sediment cores (ONW I: 6.00 m, 45°03′48″N, 100°34′39″E; ONW II: 13.35 m, 45°04′28″N, 100°35′08″E, 1219 m a.s.l.) were recovered from the western part of Orog Nuur (Fig. 1b). The core was opened, described and documented in the lab. Samples were separated and transported to (i) RWTH Aachen University for grain size and TOC analyses, and (ii) Alfred Wegener Institute for Polar and Marine Research (AWI) Bremerhaven for X-ray fluorescence scanning and X-ray powder diffraction analyses. The study here is conducted primarily on the longer core ONW II.

In total, ten radiocarbon ages were determined from bulk organic materials due to the common lack of terrestrial plant macro-remains in arid regions (Table 1). Radiocarbon dating was conducted using accelerator mass spectrometry (AMS) at the University of Erlangen-Nürnberg. The upper 24 cm of the core ONW II were not retrieved, inhibiting the assessment of the modern reservoir effect for the top of the core. The relatively high age of 12,581 ± 103 ^{14}C a BP of the uppermost dated sample from 94 cm depth indicates that the radiocarbon ages are probably significantly biased by the reservoir effect (Table 1). A study of lake sediments from Ulaan Nuur c. 250 km west of Orog Nuur determined a reservoir effect in the order of 2700–5800 a for late glacial and Holocene sediments (Lee et al. 2011). Therefore, a tentative

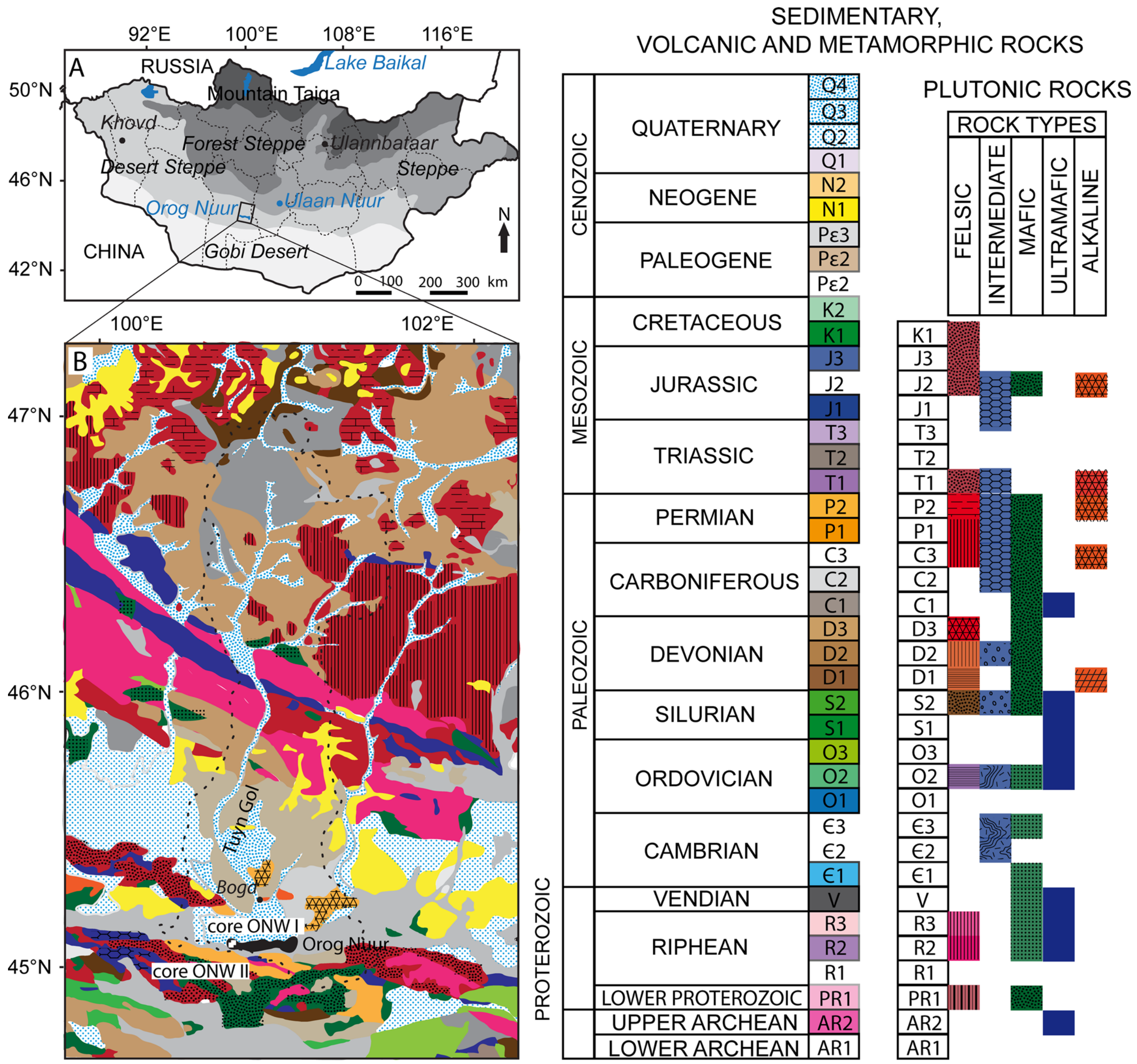

Fig. 1 Present-day distribution of geologic terranes in the Orog Nuur catchment. **a** Simplified land cover transect of Mongolia: mountain taiga, forest steppe, steppe, desert steppe, and Gobi Desert in the south. **b** Schematic geological setting of the catchment, which is marked by dashed line. Northern region of catchment is dominated with Devonian–Triassic felsic quartz syenite, granite, plagiogranite, and alkaline sediments, accompanied by patchy intermediate mafic fractions. The southern region of Orog Nuur exhibits more of mafic/ultramafic basalt and andesite-basalt rocks relative to the northern catchment. Alkaline syenite occurs sporadically in the lower reach of Orog Nuur catchments. The depositional basin is bounded by eastern Khangai in the north and the Gobi Altai Mountains in the south

assessment of the potential reservoir effect for the sediments of Orog Nuur was conducted based on expected changes in grain size, $CaCO_3$, and pollen concentration data for the periods of the LGM and a dry period encompassing the Younger Dryas (YD) from 15 to 11.3 ka, and the age of the local transition from the late glacial to the Holocene dated at Ulaan Nuur (c. 11 cal ka BP; Lee et al. 2011).

The estimation of the reservoir effect without precise independent age control is challenging, here we need to make several simplifications and assumptions to tie the ^{14}C age data from the Orog Nuur records to reference data with known age, as described below. First, the original radiocarbon age data were calibrated to calendar years with CALIB rev. 7.1 and IntCal13 (Stuiver et al. 1998; Reimer et al. 2013).

Table 1 Radiocarbon dating results for core ONW II

Core Nr.	Depth (cm)	Lab Nr.	Dating material	^{14}C ages (a BP)	δ^{13}C (%)	2σ (cal a BP) (95.4%)	Median age of the calibrated age ranges (cal a BP)[a]	Estimated anchor ages according to lithostratigraphy (cal a BP)[a]	Calibrated age based on Bayesian age-depth modelling (cal a BP)	Median age based on Bayesian age-depth modelling (cal a BP)
ONW II	94	Erl-15622	Bulk material	12,581 ± 103	− 25.4	14,325–15,192	14,876	–	5156–12,920	9102
ONW II	199	Erl-15623	Bulk material	13,242 ± 85	− 24.2	15,691–16,138	**15,918**	**11,300**[b]	8329–15,516	11,960
ONW II	271	Erl-15624	Bulk material	17,733 ± 149	− 25.4	21,042–21,819	**21,460**	**15,000**[b]	11,605–18,260	14,578
ONW II	392	Erl-15625	Bulk material	17,713 ± 180	− 24.5	20,945–21,857	**21,428**	**18,700**[c]	14,194–20,797	17,278
ONW II	571	Erl-15626	Bulk material	19,738 ± 179	− 23.8	23,344–24,150	23,767	–	17,093–24,117	20,277
ONW II	778	Erl-15627	Bulk material	21,501 ± 217	− 24.2	25,386–26,122	25,792	–	20,143–28,352	24,245
ONW II	1192	Erl-15628	Bulk material	46,103 ± 2281	− 25.4	44,908–49,914	48,202	–	31,277–43,842	37,920
ONW II	1272	Erl-15629	Bulk material	40,429 ± 1340	− 24.9	42,221–46,226	44,069	–	34,974–47,242	41,334
ONW I	386	Erl-12107	Bulk material	16,020 ± 105	− 28.1	19,049–19,560	**19,329**	**18,700**[c]	–	–
ONW I	588	Erl-12108	Bulk material	17,642 ± 112	− 23.4	21,020–21,653	21,334	–	–	–

The AMS ^{14}C ages were calibrated to calendar years with 2σ standard deviation using the CALIB rev. 7.1 (Stuiver et al. 1998) and IntCal13 (Reimer et al. 2013). According to the anchor ages based on the lithostratigraphy, a reservoir effect of ∼ 3609 ± 2168 a was subtracted from original radiocarbon ages before calibration and generation of the Bayesian age-depth model for core ONWII (Fig. 2)

[a] The reservoir effect was estimated by a comparison of determined radiocarbon ages and assumed ages of climatostratographic changes in the sediment core. The difference between the calibrated ages from Orog Nuur marked in bold and expected ages (‘anchor’ ages) for significant climate change in the region was determined at four stratigraphic levels in cores ONW I and II. The mean difference of 3609 ± 2168 a (with Std) results from the four differences of 4618, 6460, 2728, 629 a, respectively

[b] The upper and lower boundaries of a local dry period including the time of the YD event in the Valley of Gobi Lakes are dated by optical stimulated luminescence technique to 11.3 and 15.0 ka, respectively, according to nearby record of Ulaan Nuur (Lee et al. 2011; Fig. 1). The depth of 199 cm—6 cm above the upper boundary of the dry period—is corresponding to the anchor age of ∼ 11.3 ka, while the depth of 271 cm—roughly below the boundary of the dry period is corresponding to the anchor age of ∼ 15 ka

[c] The lower boundary of the ‘local LGM’ in the eastern Khangai (Otgon Tenger Uul) was determined by ^{10}Be cosmogenic nuclide dating of terminal moraine boulders to c. 18.7 ka (Lehmkuhl et al. 2016). The depth of 392 cm (ONW II)—2 cm under the lower boundary of the local LGM—is corresponding to the anchor age of ∼ 18.7 ka, which is also applied to the depth of 386 cm in parallel core ONW I

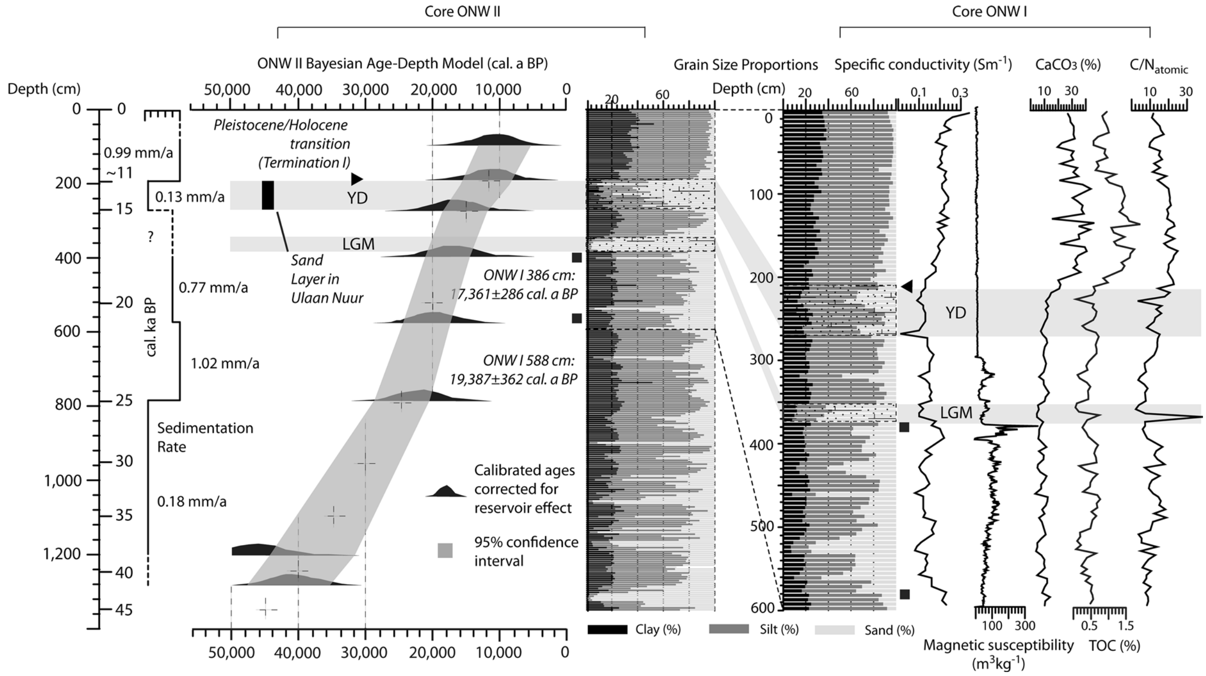

Fig. 2 Lithostratigraphy and Bayesian age-depth modelling for core ONW II. R package *Bchron* (Parnell et al. 2008) was employed. Gray shaded area represents maximum and minimum age-depth estimates based on 100,000 smooth spline fits through the calibrated age distributions (95% highest density region). The Bayesian age-depth model was further cross-validated by several independent approaches: (i) two ages from the parallel core ONW I (marked as black rectangles), (ii) sand layer and luminescence-determined age model of Ulaan Nuur (Lee et al. 2011), (iii) downcore variance of $CaCO_3$ concentration

Second, the reservoir effect was established by a comparison of the determined calibrated age data for two prominent coarse-grained sediment units in cores ONW I and II with expected ages of significant climate changes in the region. The lower sand unit was regarded to represent the local LGM while the upper unit of silty sand was considered to represent a dry period including the Younger Dryas (YD) event. Accordingly, age data for samples from near the base of the lower sand unit in core ONW I (at 386 cm) and II (at 392 cm, 2 cm below the sand layer) were compared with the expected age for the beginning of the local LGM of c. 18.7 ka determined by Lehmkuhl et al. (2016) for the eastern Khangai Mountains. Age data for two samples near the lower and upper boundary of the silty sand unit in core ONW II (at 271 cm, just below the lower boundary of the unit; and at 199 cm, 6 cm above the unit) were compared with the age of a dry period inferred from Ulaan Nuur. The beginning and termination of the dry period was determined by optically stimulated luminescence dating as 15.0 and 11.3 ka (Lee et al. 2011; Fig. 1; Table 1). All four determined, calibrated radiocarbon ages from Orog Nuur are between c. 630 and 6460 a older than the expected ages, indicating that the radiocarbon dating results from Orog Nuur are probably biased by the reservoir effect (Table 1). The mean difference between determined and expected ages with its standard deviation of 3609 ± 2168 a are therefore considered as best approximation of the reservoir effect. In the light of studies by Lee et al. (2011) and Mischke et al. (2013), a relatively high reservoir effects of the Orog Nuur record in an order of greater than 3000–4000 years is not uncommon. This age was subtracted from all original radiocarbon dating results from Orog Nuur to account for the reservoir effect. The Bayesian age-depth model for core ONW II was established using the *Bchron* R package (Parnell et al. 2008; ESM1).

Grain size analysis

The grain size distributions (GSDs) of 258 samples from ONW II and 114 samples from ONW I at a 5-cm interval were determined using a Beckman Coulter LS13320 Laser Diffraction Particle Size Analyzer. All

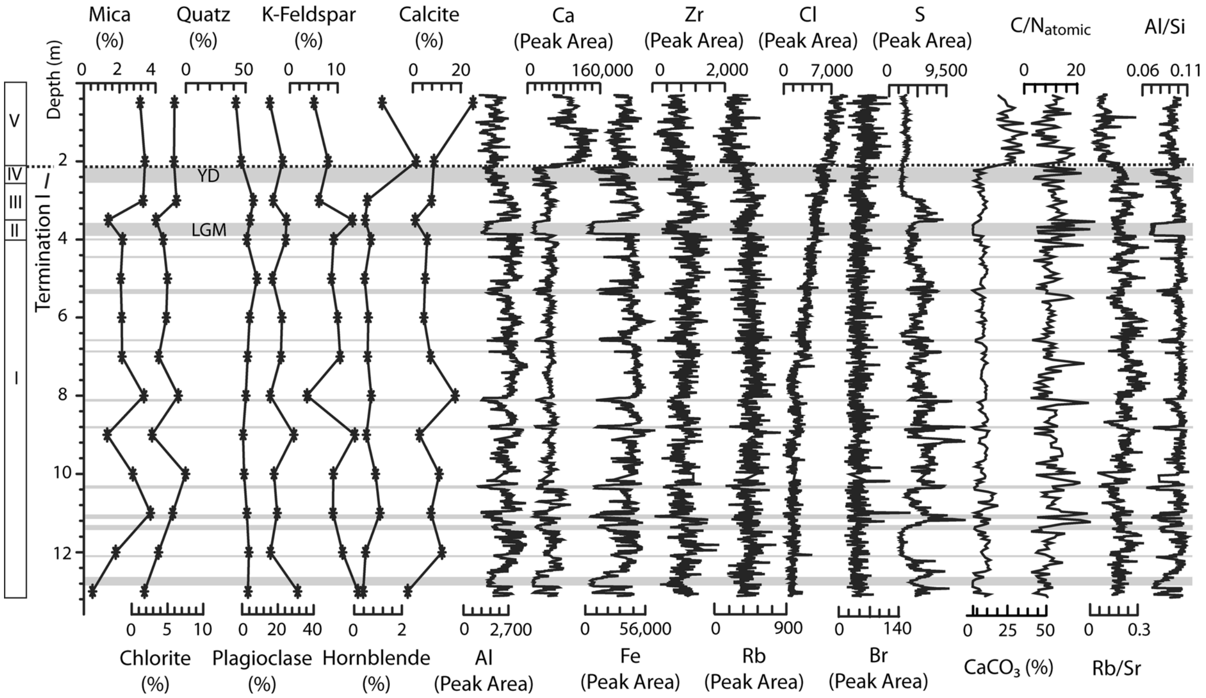

Fig. 3 Downcore variance of abundance of the major and trace elements expressed by integrated peak areas (total counts per second), accompanied by the C/N_{atomic} ratios, $CaCO_3$ content, Rb/Sr ratio (lower values = higher catchment weathering; Davies et al. 2015), Al/Si ratio (lower values = higher coarse-grained sands; Davies et al. 2015), and the XRD determined minerals in sparser intervals. Silicon and K share similar patterns as Al, whilst Mn and Co share similar patterns as Fe (ESM3). The grey bars depict the sand layers inferred from the granulometric and lithostratigraphic characteristics of the core, and the dashed line mark the transition of Termination I. The consistency between the grey bars and the elements spikes implies that the sand fractions (Factor 1 as determined by robust statistics; Fig. 4) have played a pivotal role in the alteration of bulk-geochemistry of the lacustrine sediments

measurements were performed uniformly without hydrochloric acid treatment (Felauer 2011; Schulte et al. 2016). 700 µl of 35% H_2O_2 was added to remove the organic components. Samples were subsequently dried at 70 °C for 2 days. Sodium pyrophosphate was added to avoid coagulation. The final GSD represents the average of two subsamples. Each of them was measured twice to ensure the reliability. In any case of conspicuous offsets exist between subsamples, the procedure was repeated for the sample (Schulte et al. 2016).

TOC, $CaCO_3$ and C/N_{atomic} analyses

In total 258 samples (ONW II) were dried at 36 °C for 24 h. The prepared samples in zinc capsules were analyzed in a CHNS Analyzer EA3000. The Scheibler gas method (DIN 19684) was used to calculate the $CaCO_3$ content. Total organic carbon (TOC) was computed following Scheffer and Schachtschabel (2002). The C/N_{atomic} ratios of core ONW II were calculated for the following discussion (Meyers and Lallier-Vergès 1999).

X-ray fluorescence scanning and X-ray powder diffraction analysis

The X-ray fluorescence (XRF) analysis was conducted using an Avaatech XRF Core Scanner configured with a Canberra X-Pips 1500-1.5 detector (20 s dwell time, slit 10 mm, 10, 30 keV, 300 and 700 µA) (Richter et al. 2006) at the AWI Bremerhaven. For core ONW II, in total 1335 results at a 1-cm scanning step size were retrieved. Subtraction of a background curve, application of statistical corrections for physical processes in the detector, and deconvolution of overlapping peaks were performed using a scanner equipped WinAxil package (NIOZ and Avaatech 2007). Element abundance is given in integrated peak areas (total counts per second or cps). To help discern

Table 2 Standard deviation, variance/cumulative proportion, multi-proxies loading for each factor, and communalities for each proxy generated by robust multivariate statistics

Multi-proxies	Factor 1: sand fraction	Factor 2: authigenic productivity	Factor 3: organic material	Factor 4: terrigenous input	Communality estimates
Al	− 0.249	− 0.129	–	**0.930**	0.944
Si	–	− 0.117	–	**0.911**	0.844
S	–	− 0.448	–	–	0.201
Cl	–	**0.756**	–	− 0.118	0.585
K	− 0.340	–	–	**0.935**	0.990
Ca	− 0.494	**0.780**	–	–	0.852
Ti	− 0.459	− 0.105	–	**0.826**	0.904
Cr	− 0.243	0.197	–	0.194	0.135
Fe	− 0.554	–	–	**0.773**	0.904
Rb	–	− 0.367	–	0.675	0.590
Sr	− 0.108	0.697	–	− 0.153	0.521
Zr	–	− 0.109	–	0.724	0.536
N (CNS)	− **0.804**	− 0.147	0.280	0.141	0.766
$CaCO_3$	− 0.548	**0.779**	–	− 0.244	0.967
TOC	− 0.382	–	**0.954**	–	1.056
C/N_{atomic}	–	–	**0.818**	–	0.669
Mean grain size	**0.914**	− 0.242	–	− 0.234	0.949
Clay fraction	− **0.780**	0.470	–	–	0.829
Silt fraction	− **0.926**	0.122	–	0.269	0.945
Sand fraction	**0.934**	− 0.258	–	− 0.212	0.984
Standard deviation	5.281	3.097	1.685	5.172	–
Variance proportions/%	26.4	15.5	8.4	25.9	–
Cumulative proportions/%	26.4	41.9	50.3	76.2	–

High positive or negative (> 0.75) loadings are marked in boldface. Blank values represent those loadings which are under significance level in robust multivariate statistics. Communalities for each element are computed by taking sum of the seared loadings, it can be referred to the length of the element arrows in loadings plot (Fig. 4a), a value greater than 0.90 suggests a well representative of this proxy in the statistical model. Factors 1 (26.4%) and 4 (25.9%) explain more than have of the variance, they are therefore illustrated in the biplots of Fig. 4 for further implications. More details concerning the statistics refer to Yu et al. (2016)

their environmental and/or provenance implications, the whole set of elements were further divided into four groups based on robust multivariate statistics as outlined below (Fig. 3).

To further interpret the bulk-geochemical composition of samples from different sedimentological settings, a standard X-ray diffraction (XRD) technique using a Philips X'Pert MPD diffractometer with a divergence slit using array Cu K_α radiation (40 kV, 50 mA) was employed to detect the bulk mineralogical composition of 14 samples at the depth of 50, 200, 300, 350, 400, 500, 600, 700, 800, 900, 1000, 1100, 1200, 1300 cm, respectively (Fig. 3). Minerals were identified from XRD patterns of samples at 3.34 Å (quartz), 3.24 Å (K-feldspar), 3.19 Å (plagioclase), 3.024 Å (calcite), 6.15 Å (mica), 14/7.02/4.72 Å (kaolinite-chlorite/chlorite), 3.57 Å (kaolinite) 8.47 Å (hornblende), and minor spikes at 10/5 Å (illite). The measurement was performed from 2° to 35° 2θ with scan speed of 0.02° 2θ/2 s. The integrated peak areas (total counts) of the above mineral groups were calculated and transformed into mineral percentages using the freeware MacDiff (Petschick et al. 1996). A suite of original measurements of Stein et al. (1994) and Vogt (1997) that were previously carried out at AWI were compared to ensure the comparability between the peak areas and percent calculations.

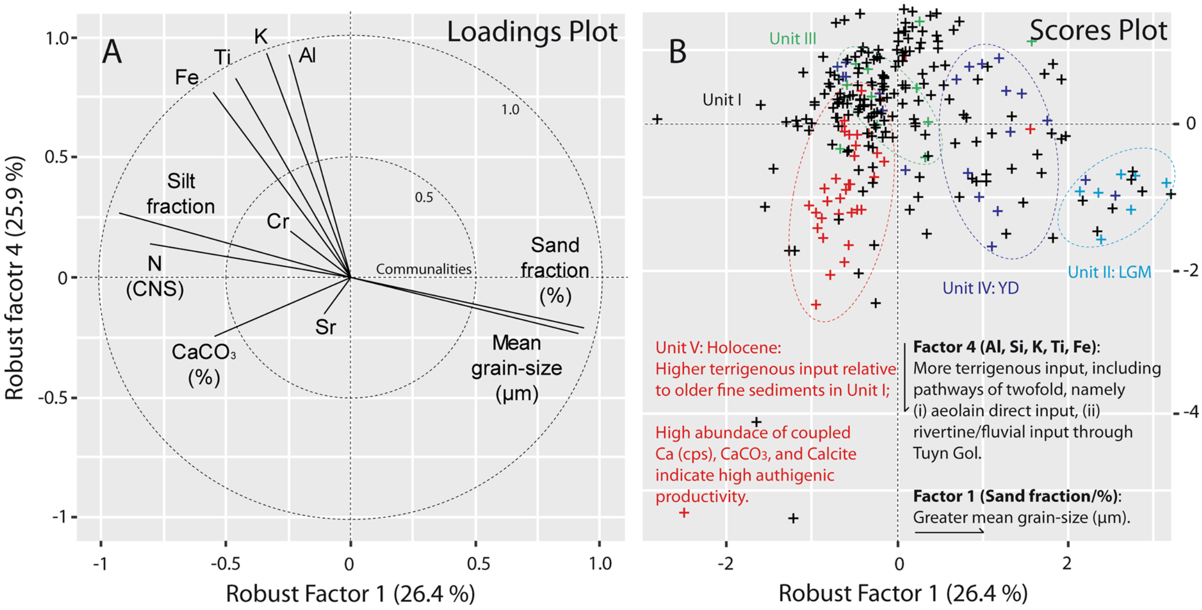

Fig. 4 Loadings and scores plot of the multi-proxy data set. **a** Loading plot of the robust Factor 1 (grain size) versus 4 (terrigenous input). **b** Score plot of the robust Factor 1 versus 4. In multivariate statistics, the maximum direction of variance is regarded as axes. Rotation is performed to get varimax rotated axis (x- and y-axis in **a**) during the analysis attempting to archive a higher loading for each elements (Table 2). Cosine of the angle between the proxies and varimax rotated axes are factor loadings, length of the arrows are corresponding to the proxy communalities. In (**b**), all units of samples are defined based on their lithostratigraphic units

Robust multivariate statistics

To provide a quantitative manner in which to segregate the whole set of multi-proxies into detailed assemblages, a robust multivariate statistical analysis is computed using the R package “*Robustfa*” (https://cran.r-project.org/web/packages/robustfa/robustfa.pdf). A detailed computing process and the manner of data interpretation were given in Yu et al. (2016). The robust evaluation parameters for each factor and sediment sample are presented in Table 2. Those elements with high positive or negative (> 0.75) loadings are shown in boldface and will be included for further discussion regarding their integrated environmental processes, provenance, and land surface processes.

Results

Lithostratigraphic units and Bayesian chronology

The radiocarbon dating of ten samples from cores ONW I and II yielded ages between 12,581 ± 103 and 46,103 ± 2281 ^{14}C a BP. Sample ages generally decrease towards the tops of the cores. The lowermost sample of core ONW II is slightly younger than the sample following 80 cm above (Table 1). According to the ^{14}C data and the application of a Bayesian age-depth model, the basal part of ONW II represents an age range between ~ 39 and 51 ka, with a median age of ~ 45 ka (Fig. 3). The Termination I has manifested remarkable consistency in a complete set of palynological, geochemical and ostracod studies (i.e. abrupt increase of pollen concentration, $CaCO_3$ abundance, and ostracod valves, respectively after the Termination I; Murad 2011) on core ONW II, and thereby validate the onset of the Holocene stratigraphy in our age model. The chronology of the core is based on the estimation of the reservoir effect as 3609 ± 2168 a. Age data for specific stratigraphic levels in the cores were compared with known climatostratographic periods in the region with sound and reliable references. This approach may introduce some bias and uncertainty. Sampled stratigraphic levels in the cores ONW I and II do not necessarily exactly represent the time of local climate periods such as the end of the dry period identified at Ulaan Nuur at 11.3 ka BP. However, probable age differences between the ‘true’ sample age and the time of the local climatostratoraphic events are regarded as reservoir effect. In the case of tying ages from other dated sections depth, offsets between ^{14}C ages and the reference ages are present, but their uncertainty in our opinion is negligible relative to the reservoir effect and its uncertainty. The wide range of the reservoir effect applied to uncalibrated ^{14}C ages propagates nonlinearly into calibrated ^{14}C ages, so that these may be seen as relatively conservative age data. The uncertainty resulting from the Bayesian model is consistent with the initially assumed age data which were used to assess the reservoir effect, also because the calibration points comfortably lie within their uncertainty range. In addition, it is to note that results of (Bayesian) age models must be seen as results of applied methods. Here we create an age-depth model is based on several well-reasoned assumptions and a relatively low limited number of ^{14}C ages. We are confident that real ages are within the given range of the age-depth model (Fig. 2). Overall uncertainty is proposed to be dominantly systematic and driven by the not precisely known reservoir effect.

On the basis of lithostratigraphic, granulometric, and geochemical characteristics, the entire sequence is delimited into five units:

Unit I (1335–390 cm; ~ 45 to ~ 19 cal ka BP)

Unit I is dominated by greyish clayey-silty sediments (on average 60–80%; Fig. 2) with intercalations of several brownish sand layers that are marked as grey bars in Fig. 3. $CaCO_3$ remains generally stable with low values (~ 10%) within Unit I, while the C/N_{atomic} ratio displays a relatively varied pattern (Fig. 3) with several laminations with values greater than 20.

Unit II (390–350 cm, ~ 19 to ~ 18 cal ka BP)

Unit II is a salient brownish coarse sand layer which is also captured by the parallel core ONW I (Fig. 2). The sand fraction ranges from 91.5 to 96.1%. $CaCO_3$ abundance exhibits extremely low values while C/N_{atomic} ratios display high values with oscillations (Fig. 2).

Unit III (350–248 cm; ~ 18 to ~ 15 cal ka BP)

Unit III is a dark greyish clayey-silty layer similar to Unit I. The sand fraction ranges from 10 to 35% with an abrupt increase in the basal part of Unit III to ~ 35% and a subsequent decrease to 10% at 283 cm. The $CaCO_3$ and C/N_{atomic} ratio depict similar patterns to Unit I.

Unit IV (248–205 cm; ~ 15 to ~ 11 ca ka BP)

Unit IV is dominated by the sand proportion (50–90%). The sand layer is also present in the parallel core ONW I and the adjacent Ulaan Nuur (Fig. 1; Lee et al. 2011). $CaCO_3$ content remains similar to Unit III, while the C/N_{atomic} ratio shows more fluctuations similar to Unit II. Throughout Unit IV, the S content exhibits low values (Fig. 3).

Unit V (205–25 cm; < ~11 cal ka BP)

Unit V is characterized by fine sediments with the highest clay proportion (30–50%) and the lowest sand fraction (1–10%). A sharp increase in $CaCO_3$ (calcite; Fig. 3) and concomitantly diminished S contents are present in Unit V. C/N_{atomic} ratios decrease from ~ 20 to < 10 upward and increase incrementally approaching the top of the core.

Elements/minerals downcore variance and multi-proxy assemblages revealed by multivariate statistics

The major and trace element concentrations, as well as mineral compositions throughout the core ONW II were plotted against the depths and stratigraphic units (Fig. 3). In light of the multivariate statistics (Fig. 4; Table 2), the whole set of elemental compositions and other proxies are evaluated using a robust factor analysis. They are divided into four factors: (1) Factor 1 (variance proportion: 26.4%) is positively correlated with mean grain size of the sediments and negatively correlated with the N content of the sediments. (2) Factor 2 (15.5%) exhibits significantly high loadings of Cl, Ca and $CaCO_3$ content. In general, Ca and Sr concentrations display a unique pattern that resembles $CaCO_3$ and hornblende, with relatively low abundances throughout the late Pleistocene and sharp increases after Termination I. Cl exhibits a long-term trend of upcore increase along with superimposed fluctuations. In general, the factor is an indicator for the authigenic productivity of the lake system. (3) Factor 3 (8.4%) delineates higher loadings for TOC and C/N_{atomic} and an insignificant correlation with elemental compositions and grain-size composition. (4) Factor 4 (25.9%) has significantly high loadings of Al, Si, K, Ti, and Fe. This set of elements exhibits higher abundance in Units I, III and V (relatively lower in Unit I), while the contents in Units II and IV are markedly lower. They share broadly similar patterns to mica and chlorite. This factor is explained as terrigenous input brought by two pathways: (i) riverine inflows via Tuyn Gol, and (ii) quasi-constant aeolian inputs. In addition, note the relatively high variability of the element concentrations of, in particular, Unit I (Fig. 3), which may result from the frequently occurrence of sand layers as illustrated by the grey bars in Fig. 3. In this scenario, insight into the bulk-geochemistry of each unit is more readily obtained in the dispersion plots, wherein Units I and III share broadly similar median values and upper/lower quartiles (Fig. 3; ESM2). Factors 1 (26.4%), 4 (25.9%), and 3 (15.5%) explain ~ 70% of the multi-proxy variations; they are the primary governing factors for the sediment bulk-geochemistry.

In terms of the minerals, mica, chlorite, quartz, plagioclase, K-feldspar, hornblende, and calcite are determined at coarser intervals throughout the core ONW II (Fig. 3). Amongst those minerals, (1) quartz and plagioclase display only minor variation through the core; (2) mica and chlorite exhibit a highly coupled pattern that has higher values in the lake phases (Unit I, III, and V); (3) calcite and hornblende have a similar pattern with higher values specifically in the Holocene (Unit V) relative to the Pleistocene units; (4) K-feldspar denotes a broadly reversed pattern compared with that of mica and chlorite, and appears to have a higher content corresponding to the sand layers (grey bars in Fig. 3). In general, the set of XRD data shed light on the general mineralogical composition of the studied core, and thereby aid in further interpretation of the XRF scanning data.

Discussion

Evaluating the quality of the X-ray scanning data

As mentioned above, the retrieved XRF core scanning data are expressed in semi-quantified integrated peak area/total counts per second (cps) without conversion to oxide wt% or molar abundance.

Amongst the entire suite of elements, Ni, Cu, Zn, Ga, Br, Au, Pb, and Bi have a relatively high error margin compared to their measured peak areas. They are therefore removed from the multivariate statistics (ESM3). In the statistical report (Table 2), the proxies that are under significance level are ruled out for the following discussions as well. The remaining set of elements show measured peak areas that are well above the theoretical detection limit of the Avaatech XRF scanning infrastructure (Richter et al. 2006; NIOZ and Avaatech 2007). Certain low count rates (in particular for light elements such as Si) may be ascribed to intervals with very coarse-grained sediments such as those in Unit II and Unit IV in this core (Richter et al. 2006; Shanahan et al. 2008; Weltje and Tjallingii 2008; Ohlendorf et al. 2015). However, concerning the XRF scanning technique and its applications on marine, fluvial, and lacustrine sediments, in general, the precision of data obtained by XRF core scanning is not significantly altered by grain-size variations or texture of sediments (Bertrand et al. 2015; Jarvis et al. 2015). They correct the XRF peak areas for water content and grain size, which only slightly improves the correlation between XRF peak areas and Inductively Coupled Plasma Mass Spectrometry (ICP-MS) determined bulk-geochemistry concentrations. This improvement is, however, relatively minor; the difference between the correlation coefficients is never significant at $p < 0.05$ level (Bertrand et al. 2015). Furthermore, Schillereff et al. (2015) demonstrate for the first time that the employment of different XRF scanning instruments (mainly Avaatech and Itrax, etc.) yields similar elemental patterns, implying a robust and sound quality of the retrieved data. Meanwhile, Dulski et al. (2015) analyzed parallel subsamples using XRF scanning and ICP-MS, also revealing a systematic relationship between the scanned data and element concentrations.

In terms of late Quaternary lacustrine sediments, although diagenesis may indeed exert certain influence on the fate of bulk composition (Johnsson 1993), it is, however, a less crucial aspect compared with the alteration of paleoenvironment and source lithotypes in the entire catchment system. Pettijohn et al. (1973) concluded that due to the limited burial time, calcite cements along with the negligible quartz overgrowths are virtually the only diagenetic overprints. Thus, source terranes, paleoenvironment-induced weathering and transportation adaptations are more likely the governing factors for the late Quaternary lake sediments. On this account, the following discussion is generally demarcated and outlined in twofold: (i) the paleoenvironmental (weathering, land surface processes) implications, and (ii) provenance signals.

Governing factors for sediment bulk-geochemistry

In the marine realm, researches have been systematically undertaken to examining the sediment bulk-geochemistry and its environmental interpretations (Calvert and Pedersen 2007; Diekmann et al. 2008; Martinez-Ruiz et al. 2015). It has been suggested that assemblages of the elements exhibit specific indications of the redox condition (Mn and Co), diagenetic processes (Fe), authigenic productivity (Al and Ba) and the allogenic aeolian/fluvial inputs (Zr and Rb) during sedimentary processes. Here, in the lacustrine realm, a holistically refined view of the governing factors of sediment bulk geochemistry, taken in consideration of other multidisciplinary proxies, is employed using robust multivariate statistics as a prerequisite for the following discussions.

Factor 1 (26.4%): grain-size variation of the lacustrine sediments

This factor has the highest proportion, 26.4%, as determined by the factor analysis (Table 2). In arid central Asia, aeolian sand plays a primary role in the terrestrial context (Kazancı et al. 2016). The abundance of the sand percentage (63–2000 µm fractions) is also well presented as low values for Al, Fe, and Al/Si ratios (Fig. 3). In order to examine the sand-induced influence on the bulk geochemistry, all samples are plotted in the scores plot based on the multivariate statistics (Fig. 4b). Samples with a great contribution from (aeolian/fluvial) sand fractions particularly approach the positive end of Factor 1, while those samples of clay or silty-clay sediments are scattered at intermediate to negative positions on the Factor 1 axis. Interestingly, all coarse-grained samples from the Unit II (LGM) strata are relatively clustered, while those from the Unit IV (YD) are more scattered. This may be because the Unit IV strata correspond to a playa phase that is more frequently influenced by the riverine input (mixture of both fluvial sands and finer suspended river sediments; Fig. 2), instead of predominantly coarse-grained sands as in Unit II. It must also be remembered that the sediment bulk-geochemistry is not solely a reflection of the sediment grain-size composition, indicated by the fact that that no elements in Factor 1 are well above the significance level (Table 2).

Factor 2 (15.5%): authigenic productivity of the saline/alkaline lacustrine environment

Factor 2 has significantly high loadings of Cl, Ca, and $CaCO_3$ (Table 2). Ca is generally included in carbonates which are also common minerals in lacustrine environment (Tucker and Wright 1990). Calcite, low-Mg calcite, and rarely occurring aragonite are generally authigenic precipitates in lake sediments while dolomite (along with quartz and feldspar) could be regarded as detrital input (Sinha et al. 2006; Wünnemann et al. 2010). In core ONW II, the abundance of calcite, Ca and $CaCO_3$ share analogous patterns, implying that in this study Ca is present mainly as calcite, and Unit V (Holocene) depicts notably higher authigenic productivity relative to the late Pleistocene epoch (Fig. 3). In contrast, Al and Si display lower values in the Holocene, acting as an analogue for plagioclase and K-feldspar (Fig. 3), suggesting a non-productivity signature. Therefore, compared with the marine pelagic realm, Al is not an indicator for the authigenic productivity. On the other hand, Sr has relatively high loadings, but its content variation is still under significance level (Table 2). Sr behaves quite similarly to Ca due to their similar hydrogeochemical characteristics (Calvert and Pedersen 2007; Kylander et al. 2011). Likewise, Davies et al. (2015) also suggest that the presence of Ca and Sr is commonly associated with authigenic carbonate minerals in catchments located in arid and carbonate environments. In the lacustrine realm, halite is a ubiquitous species that may partly be generated by re-precipitation from pore solutions (Sinha et al. 2006). Similar to halite, the halogen element bromine may also be readily incorporated in halide salts. The upcore increase of these halogen elements (Fig. 3) implies a higher salinity/alkalinity approaching the upper part of core ONW II. Particularly in the Holocene, this high salinity and/or alkalinity are corroborated by the significantly elevated $CaCO_3$ abundance (Fig. 3).

In addition, Sulfur is in part negatively correlated with the Factor 2, albeit under the significance level (Table 2). Sulfur might be present as sulfate (gypsum and anhydrite), sulfide, and pyrite (Millot 1970). As illustrated in Fig. 3, S exhibits higher content in Units I-III, low values in Unit IV and is slightly elevated in the uppermost unit. In the late Pleistocene units, the less disturbed lake states may have led to a relatively higher content of sulfide and pyrite precipitation at the sediment–water interface. The sulfide minerals were then almost entirely oxygenated when exposed in the sand/playa layer and subsequently produced sulfate precipitation in the alkaline environment of Unit V. Alternatively, the sporadically deposited gypsum and mirabilite in such a cold, dry lake system may also account for these S spikes determined in Fig. 3. However, above all, the insignificance level of S loading for Factor 2 (Table 2) suggests that sulfide or sulfate mineral genesis is of minor importance for the bulk-geochemistry. This is also corroborated by clear evidence that above mentioned minerals are not detected by the XRD analysis in this study (Fig. 3).

Factor 3 (8.4%): organic material content

Factor 3 is represented by significantly high loadings of TOC and C/N$_{\text{atomic}}$ (Table 2). The TOC content incorporated in the core sediments is relatively low (Fig. 2). The coupled variation of TOC and C/N$_{\text{atomic}}$ values implies that the lacustrine system has merely minor biogenic activity, and that the low content of the organic matter incorporated in the core was brought into the depocenter via allogenic fluvial processes, and lake-derived organic matters was partially mixed into the sediments, given that C/N$_{\text{atomic}}$ ratios greater than 20 indicate allochthonous input into the lacustrine system (Meyers and Lallier-Vergès 1999).

Factor 4 (25.9%): terrigenous components via riverine input and quasi-constant aeolian input

Factor 4 has high loadings for Al, Si, K, Ti and Fe (Table 2). Clay or silty-clay is the predominant

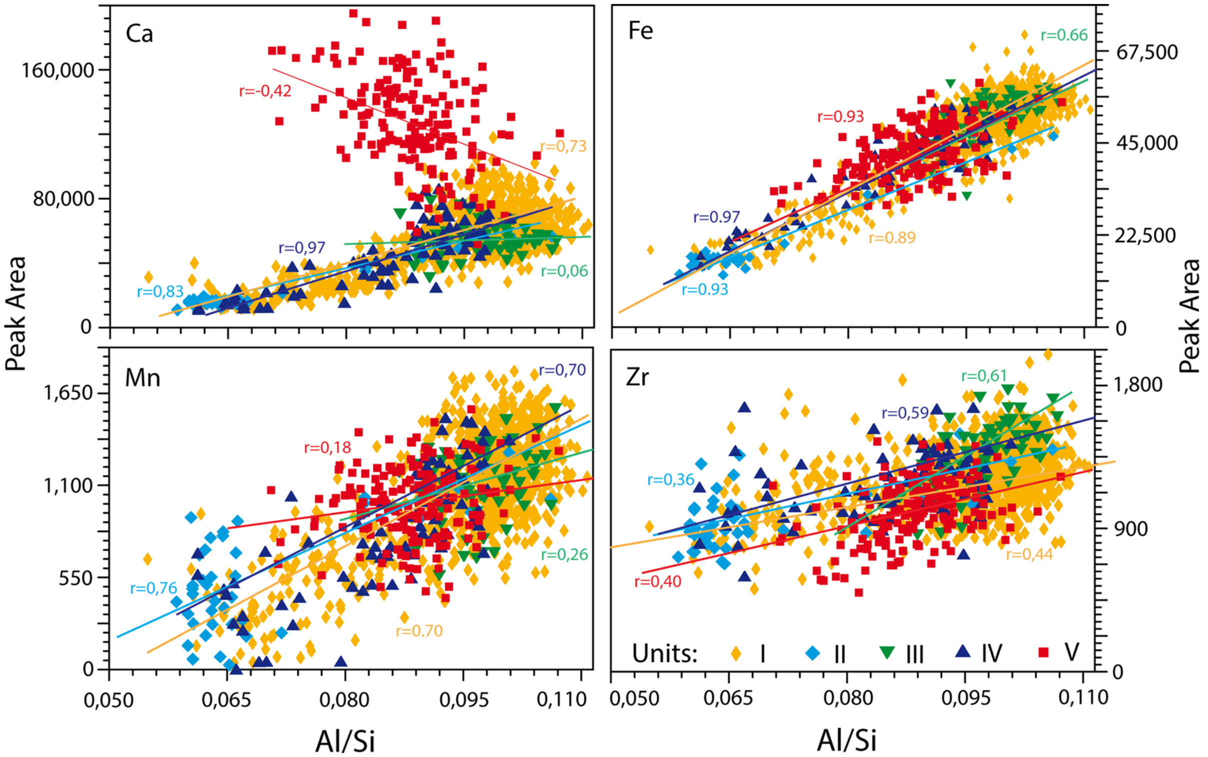

Fig. 5 Bivariate plots of major and trace elements in peaks areas (*y*-axis) against Al/Si (*x*-axis) according to their stratigraphic units. Al/Si ratios indicate generally the grain-size compositions of the bulk sediments, which display lower values/spikes according to the coarse-grained sand layers (Fig. 3). The biplot of Ca versus Al/Si seems like a useful tool to properly discriminate the instinct (i) source rocks changes, and (ii) authigenic productivity in comparison with the late Pleistocene units. This distinct Holocene samples characteristics are more clearly elaborated in the scores plot of Fig. 4b

sediment in the lacustrine environment (Millot 1970). The fine detrital matrix formed mainly from the weathering decomposition of the primary aluminosilicates, which are the main host for Al (Calvert and Pedersen 2007). On the other hand, Al may also be incorporated in feldspar and micas (Millot 1970). In core ONW II, Al and Si display broadly identical patterns (Fig. 3), indicating a close link due to similar host minerals in fine sediments, either in a feldspathic structure or as a set of clay minerals in water bodies (Millot 1970). In addition, in an arid context such as the Gobi Desert, in situ evaporated alkaline water was reported to be rich in Si and depleted in Al (Millot 1970), which may account for the lower Al abundance in Unit V when calcite or carbonates are the predominant minerals in the water body (Fig. 3). In addition, several works suggest that the organic content in a lacustrine environment may exert strong influence on the Al abundance (Davies et al. 2015). However, in the arid context of the Orog Nuur, the TOC values are broadly no greater than 2–3% (Fig. 2), thus making the above Factor 2 less important.

Due to the complex characteristics of its provenance ranging from fine clays to coarse sands (Yu et al. 2016), Si presents an unclear indication of the grain-size composition (unpresented in Factor 1; Table 2). Indeed, aeolian sands exhibit higher amounts of SiO_2 (Yu et al. 2016). However, in this context in Orog Nuur, Units II and IV may not be ascribed to purely aeolian sand. Grain size alone cannot be precisely used to conform that the coarse-grained layers in this study are purely aeolian sands (Conroy et al. 2013). In a recent study on the Gobi Desert archives, SiO_2 content was found to be 71% (aeolian sands), 55% (lacustrine clay), 47% (fluvial sands), 69% (sandy loess), and 36% (alluvial gravels), respectively (Yu et al. 2016). This relatively lower Si content in the coarser-grained fluvial sand layer is also suggested by Dulski et al. (2015) based on scanning of the Piànico paleolake sequence. Likewise, Hunt et al. (2015) also demonstrate that increasing grain-size composition will not necessarily result in an elevated Si value. Thus, the fluvial sands may indeed display lower Si abundance relative to lacustrine clays in the core. In addition, as given in Yu et al. (2016), the sand fraction of the fluvial sands may be as high as that of the aeolian sand, albeit more spikes in finer fractions may be observed in the granulometic curves of fluvial sands. Thus, the complex provenance of lacustrine sediments from both coarse sands and alluminosilicate clays leads us to assume that the relatively coarse-grained layers (Units II and IV) may be largely attributed to fluvial transportation, rather than purely aeolian sands. On the other hand, in this aeolian sand and silt source region, the fluvial system normally experiences multi-cycle deposition of the coarse material. The SiO_2 values in this aeolian material show a significant decrease through long-term weathering processes (Bridge and Demicco 2008), rendering a considerably lower SiO_2 abundance of the fluvial sands detected by the core scanning in this study. Multi-cycle deposition would account for the relatively lower SiO_2 values in those coarse-grained layers relative to the lacustrine clays in other units. Furthermore, the various Al/Si ratios through the core indicate that the Si pattern is also not governed by the terrigenous aluminosilicate constituents (Fig. 5; Richter et al. 2006), demonstrating a twofold, mixed provenance for Si: (i) quartz in aeolian sands, and (ii) fine-grained terrigenous aluminosilicates.

In this study, K displays a divergent variance pattern compared with Ca and reveals convergent characteristics with Si, Al, and Fe (Figs. 3, 4). The behavior may result from mechanisms suggested by Millot (1970), namely, in young aqueous sediments, Ca is preferentially fixed into carbonates while K enters silicates. Furthermore, as illustrated in Fig. 3, the most likely host for K in the Orog Nuur sediments is K-feldspar with partial contributions from micas or chlorite, which may all be associated with allogenic fluvial inputs, as well as the aeolian processes (Costa et al. 2014).

In core ONW II, hornblende and micas are the potential hosts for Iron (Fig. 3). In general, hornblende is the main constituent of certain mafic source terranes in the catchments (Fig. 1b) and has weak resistance to weathering (Millot 1970). Consequently, decomposed and retained hornblende together with micas all concentrate in fine clay sediments which are liable to be transported into the Orog Nuur by hydraulic flow and/or mass movement (Nesbitt and Young 1996) from southern alluvial fans (Fig. 1). In general, Fe has two modes of occurrence, namely the trivalent state and bivalent state when it accompanies Mg or K (Millot 1970). As illustrated in Fig. 3, Fe acts in a manner analogous to Al and Si. Thus, rather than primary hornblende, Fe is mainly found in the micas and chlorite in the clayey sediments, which seems to be the same case with Ti, Rb and Co (Fig. 3). Due to the short burial time and resulting weak diagenetic influence, Fe may not be an indicator of diagenetic processes in the lacustrine realm.

Furthermore, several other elements share similar patterns as that of the above elements, they illustrate insignificant loadings for Factor 4. (1) Zirconium: there is ample evidence that Zr is relatively stable and is almost exclusively mechanically transported and fractionated (Pettijohn et al. 1973). Mukherji (1970) determined that in an acid aqueous media, Zr may also exist in polymeric species, e.g., zirconyl halides in the case of higher Cl anion abundance (Fig. 3). However, in terms of alkaline environments with higher concentrations of calcite or carbonate (higher abundance of $\left[\mathrm{HCO}_3^-\right] + 2\left[\mathrm{CO}_3^{2-}\right]$; Chilingar et al. 1979; Dapples 1979), zirconyl halides seem not to be the host for Zr. Here, the downcore Zr variance reveals no association between sand fractions and Zr abundance. However, it displays certain links with the quartz, plagioclase and K-feldspar abundance throughout the core, implying that Zr may be correlated to the precursor lithotype-governed allogenic fluvial clastic input, but is not necessarily a faithful recorder of aeolian input (Sinha et al. 2006). (2) Manganese: in spite of the two sand layers (Units II and IV), the lacustrine phase throughout the core depicts quasi-constant Mn abundance. In general, insoluble oxi-hydroxides (Mn(III) and Mn(IV) ion) occur in oxygenated environments while soluble Mn(II) occurs in anaerobic environments (Calvert and Pedersen 2007). Thus, in terms of higher lake levels with suboxic to anoxic water bottoms, more soluble Mn will be readily incorporated into the carbonate lattice and thereby share variance patterns similar to Ca or $\mathrm{CaCO_3}$, which seems largely untenable in this study (Fig. 3). The Orog Nuur therefore represents a frequently riverine inflow-disturbed shallow hydrological environment, rather than a stagnant water body. (3) Cobalt: the element Co behaves similarly to Mn and is generally enriched in clayey deposits (Costa et al. 2014). Both Mn and Co are therefore depleted in sand layers (Fig. 3). A slightly lower value in Unit V can be observed with respect to Co, albeit the broad pattern remains analogous to Mn. This lowering may be ascribed to the sensitive response of the elements to the slightly decreasing mica abundance (Fig. 3).

In summary, Factor 4, represented by Al, Si, K, Ti, and Fe, indicates the allochthonous input into the lacustrine system. This terrigenous input implication is consistent with several other works, including Kylander et al. (2011) and Davies et al. (2015).

Biplots of elements and scores plot as indicators of a distinct provenance signal and high authigenic productivity of the lake system in the Holocene

There is broad consensus that rare earth elements (REE), which are rarely influenced by diagenesis and metamorphic processes, are common indicators for provenance change (Pettijohn et al. 1973). Here, in terms of the dominating mudstone, ratios between major and trace elements were computed in an attempt to examine the possible lithotype signatures (Fig. 5). As postulated by Pettijohn et al. (1973), the Al/Si ratio is the commonly applied value in discriminating the provenance of sandstone and mudstones. In general, higher Al/Si denotes more clayey or detrital aluminosilicates while the quartz-rich sandstones have low Al/Si ratios due to the virtual absence of clay-bearing silicates (Davies et al. 2015).

Distinct assemblages related to the lithostratigraphic units are discriminated in the biplots against Al/Si (Fig. 5). Three main groups have been recognized: (i) Fe (K with similar pattern) abundances are broadly altered by silicate contents in authigenic mud and allogenic fluvial clastics brought by the Tuyn Gol. Due to the lack of a clay fraction, the Last Glacial Maximum (LGM) sediments (Unit II) are distinctly distributed with low Fe and Al/Si values, whereas the mud dominant sediments from Units I and III occupy the opposite end of the biplot. Furthermore, apart from the lacustrine sediments in this study, the quasi-linear regression ($r = 0.66$–0.97) pattern between Al/Si and Fe was also delineated in the sandstones and argillites, wherein both depositional conditions and provenance fingerprints might have been incorporated (Roser and Korsch 1988); (ii) Mn (Zr and Co with similar patterns), similarly, is also governed by clay and silt fractions. However, through sand-dominated sediments may confound the pattern of Mn (Fig. 5), data points of the LGM sediments (Unit II) are more scattered compared with those of Fe. The entire set of data points is therefore less linearly correlated relative to the first group of elements. In addition, as stated above, the whole suite of samples in the biplot of Zr versus Al/Si present a slightly more horizontal and scattered regression, implying that Zr is hosted in both clay enriched and depleted sediments, which might have complicated the biplot pattern; (iii) Ca appears to be the distinct element that allows us to discriminate between late Pleistocene and Holocene signatures. Before Termination I, the sediments exhibit a virtually linear regression in a manner analogous to Fe, suggesting a quasi-consistent alteration kinetics governed by the clay and silt fraction input (Fig. 5). Nevertheless, although they share similar granulometric compositions, the Holocene sediments in Unit V exhibit distinctly higher Ca values relative to the granulometrically similar Units I and III ($r = -0.42$) (Fig. 5). On the other hand, the LGM and Younger Dryas sand layers (Units II and IV) represent distinctly different patterns, namely the Younger Dryas sediments are more scattered relative to LGM sediments regarding the Al/Si axis. Unlike the dominantly playa condition during the LGM, the Younger Dryas may have been subject to frequent riverine inflows, resulting in a broader covering of mud-, silt- to sandstone suites (Fig. 2). As a consequence, compared with those in Unit II, the set of Unit IV data points is more scattered in Fig. 5.

The disparate provenance signatures and authigenic productivity of the Holocene sediments

The set of late Pleistocene sediments exhibits coherent regression patterns in the biplots (Fig. 5), indicating insignificantly alteration of source lithotypes through Units I-IV. This quasi-constant provenance delivery/authigenic productivity through Unit I to IV is also documented in the broadly unbiased quartz, plagioclase, hornblende and minor biased Rb/Sr ratios (catchment weathering) throughout the late Pleistocene (Fig. 3). Apart from Ca, all of the above three groups of elements display a tendency of quasi-linear regression which is altered by the amount of clay and silty-clay proportions, albeit Zr is slightly biased and scattered due to contributions from both finer and coarse sand fractions. The constant delivery of riverine inflows during the lake phase may have transported the felsic and weathered intermediate or mafic plutonic rocks into the Orog Nuur (Fig. 1b), although this phase was interrupted by two desiccated playa periods (the local LGM and Younger Dryas) with a sporadic or cessation of riverine inflows. Alternatively, in this hyperarid environment, airborne material is a permanent, vital input for the catchment depocenter. The minor variance of quartz and plagioclase content implies that the aeolian activity that conveyed coarse-grained sediments into the Orog Nuur catchment basin was quasi-constant through the late Quaternary. Likewise, as demonstrated by robust multivariate statistics, in the context of the Eijina Basin, there is no sharp variation of aeolian sands input through the late Quaternary (Yu et al. 2016), albeit the LGM might have been subject to a slightly higher aeolian deflation in the arid central Asia (Nilson and Lehmkuhl 2001). This amount of airborne material was thus incorporated into the sediment trap at a quasi-constant rate, in spite of the lacustrine setting, playa, or other land surfaces. Thus, the sharp increase of Ca since the very beginning of the Holocene seems not to have been caused solely by the quansi-constant aeolian activity.

From the onset of the Unit V, both hornblende and $CaCO_3$ demonstrate a coeval abrupt increase. This phenomenon is also documented in calcite and Ca (peak areas) (Fig. 3). The distinct behavior of Ca in the Holocene sediments is also properly depicted in the biplot against Al/Si (Fig. 5), as well as the scores plot revealed by robust multivariate statistics (Fig. 4b). All of the evidence corroborates the theory that the past environment is not the sole governing factor exerting influence on the sediment bulk-composition, and that prominently different source lithotypes and/or higher authigenic productivity may have existed before and after Termination I. This different provenance may be attributed to twofold pathways given that the catchment basin is intimately linked to the higher catchment via the Tuyn Gol: (i) in the stadial (Younger Dryas event) of the late glacial period, the glacial-pluvial debris accumulated in the higher Khangai Mountains may not have been subject to abrasion and transport into the Orog Nuur. Subsequently, immediately after Termination I, due to climate amelioration-induced deglaciation and the hydrodynamically strengthened riverine inflows, abrupt increases of clastic minerals were available for transport into the Orog Nuur (Fig. 1b), resulting in a sharp increase of the Ca, calcite, and hornblende abundance in the Holocene, as well as the distinct biplot pattern of Ca versus Al/Si (Figs. 3, 5). Furthermore, this increased weathering and fluvial input is corroborated by the negative values of Factor 4 (high terrigenous input) of the Holocene samples in the scores plot (Fig. 4b) and the decreased

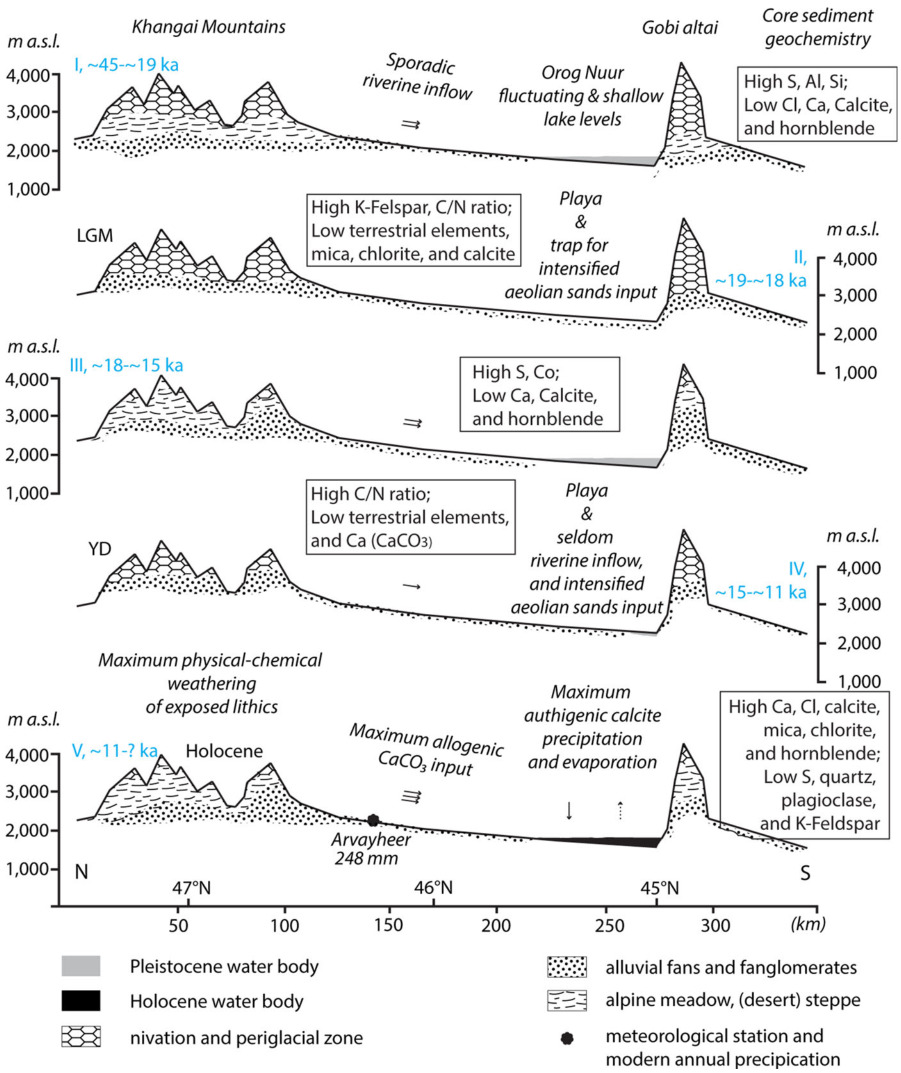

Fig. 6 Schematic model of the integrated past environmental change, land surface processes and provenance signals (carbonate geochemistry) of the Orog Nuur catchment over the last ~ 45 ka. The eastern parts of Khangai Mountains (higher reach of the Orog Nuur catchment) with altitudes between 3500 and 3700 m asl have no modern glaciers. More details regarding glacial and vegetation developments in the catchment are given in Lehmkuhl and Lang (2001), Rother et al. (2014), and Lehmkuhl et al. (2016). Distinct geochemical signals for each phase are shown in ESM4

Rb/Sr ratios of the Holocene samples (Fig. 3; Davies et al. 2015). (ii) Due to the temperature amelioration and better moisture conditions, markedly intensified chemical weathering (decrease of Rb/Sr) and denudation (increased mica, chlorite, and hornblende contents) occurred in the upper catchment of Orog Nuur, where the source terranes were broadly occupied by felsic/alkaline and patchy mafic plutonic rocks (Fig. 1b, 3). In addition, as suggested by Millot (1970), when hypersaline brines reach saturation, alkaline earth carbonates will be the first precipitates followed by calcite and aragonite. Thus, an immense amount of alkaline carbonates and subsequent authigenic calcite have been generated from the felsic and alkaline precursors, causing a distinct alkaline environment (higher authigenic productivity) in the Holocene. Thus, only the biplot of Ca versus Al/Si has rendered a sound and distinct picture of conditions of the Holocene relative to late Pleistocene sediments.

In summary, influences from the integrated past environment (weathering and land surface processes) and provenance signals cannot be separately discerned in the arid context. They more likely represent inherently intercorrelated mechanisms regarding the bulk-geochemistry of the lacustrine sediments (Fig. 6).

Summary of coupled paleoenvironmental, weathering, catchment land surface processes, and provenance signals over the past ~ 45 ka BP in the Orog Nuur catchment

The overall knowledge gained above has allowed gleaning of the hydro-geochemical implications of the Orog Nuur water body, as well as the reconstruction of paleoenvironmental conditions and provenance signals in the drainage catchment (Fig. 6).

Unit I (~ 45 to ~ 19 cal ka BP): shallow to lentic water body, moderate catchment weathering

Ample proxy and modelling evidence illustrates that it was generally humid in arid northwestern China over MIS 3 (Herzschuh 2006; Yu et al. 2007). It has been suggested that this may have been caused either by the strengthening of the Asian moisture-laden monsoon or by a strengthened moisture supply by the westerlies (Yang and Scuderi 2010). This enhanced moisture supply is documented in the Orog Nuur sediment core by high amounts of clay and silt, and is also indicated by a high abundance of the minerals mica and chlorite that are fluvially transported to the lake. Factor 4 elements, plagioclase, and K-feldspar retain generally high levels in Unit I, indicating allogenic fluvial input linked to adjacent source lithotypes in the catchment (Fig. 6). On the other hand, however, several intercalated sand layers with corresponding spikes in the C/N_{atomic} ratio point to sporadic desiccation of the water column and abrupt fluvial-induced allogenic terrestrial input. The depths of these sand layers (playa phases) exhibit broad consistency with the spikes in the elemental variances and the Al/Si ratio (Fig. 3). Apart from the sand layers, most phases in Unit I reveal a weak reducing environment as inferred from the Mn abundance (Fig. 3). A moderate weathering rate is demonstrated by the largely higher values of the Rb/Sr ratios throughout Unit I. In summary, Unit I developed in a humid environment with regular riverine inflows of the Tuyn Gol. Throughout the time period of Unit I, the water body was generally shallow and sporadically converted into playa conditions (Fig. 6). This generally humid phase in MIS 3 is corroborated by low dust supply in the northwestern Pacific pelagic sequences (Leinen 1989; Nilson and Lehmkuhl 2001).

Unit II (~ 19 to ~ 18 cal ka BP): playa phase and minor riverine inflow

This unit, related to the global LGM, is represented by a massive sand layer that marks an abrupt deterioration of the hydro-environment in the catchment (Fig. 6). The Orog Nuur was completely desiccated and changed to a playa environment, which served as an allogenic dust sink with ephemeral alluvial/fluvial deposition. In a modern context, aeolian silts and mobile dunes were generally accumulated in the (winter monsoon) downwind direction, namely the southeastern section of the Orog Nuur (Lehmkuhl and Lang 2001). The Factor 4 elements, mud clay, and fluvial clastic bearing minerals mica, chlorite, plagioclase, and hornblende all exhibit drastically declining contents due to the virtual absence of argillaceous sediments (Fig. 3). Conversely, allogenic K-feldspar displays an abrupt increase related to the sharply increased contribution of feldspar-bearing sand. The C/N_{atomic} ratios with broadly greater values than 20 also suggest a more frequent input of allogenic matter. The slightly reduced redox condition was broken down, as shown by extremely low concentrations of Mn (Calvert and Pedersen 2007; Wirth et al. 2013). The in situ weathered materials from the higher catchment in the Khangai Mountains were preserved locally due to reduced fluvial transport capacity, and thus were seldom transported into the Orog Nuur.

Unit III (~ 18 to ~ 15 cal ka BP): shallow saline lake, moderate weathering in higher catchment

This period corresponds with the commencement of the last deglaciation in the southern Mongolian Plateau. Climate amelioration after the LGM led to the melting of glaciers (Rother et al. 2014) in the higher Khangai Mountains and resulted in a significantly raised amount of riverine inflows into the Orog Nuur (Fig. 6; C/N_{atomic} exhibits slightly higher values relative to Unit I). The water body was instantly recovered to a state that is comparable with hydrological conditions prior to the LGM. The relatively stagnant environment is also demonstrated by high Mn abundance and low C/N_{atomic} ratios (Fig. 3). The Factor 4 elements Si, Al, and Fe exhibit similar abundances relative to those in Unit I, suggesting analogous hydro-geochemical and moderately higher catchment weathering conditions (Figs. 4b, 6). A slightly increased Cl abundance implies raised salinity of the water body in contrast to Unit I (Sinha et al. 2006). In contrast, Factor 2 proxies Ca, calcite, and $CaCO_3$ are low compared to the older late Pleistocene units, indicating a broadly unchanged authigenic condition within the lake system. Furthermore, similar Rb/Sr ratios relative to those in Unit I also reflect a largely unchanged weathering intensity in the catchment.

Unit IV (~ 15 to ~ 11 cal ka BP): playa phase with slightly more riverine inflows relative to LGM

This unit again, as in the LGM, is represented by a sand layer (Fig. 4b). It corresponds to a climate deterioration episode associated with the late glacial Younger Dryas event. Although the Orog Nuur system did not completely turn into a playa system as during the LGM (Unit II; Fig. 4b), it experienced repeated desiccations giving rise to the deposition of coarse sands brought in by fluvial and aeolian processes (Fig. 6). The sharp decrease in clay and silt–clay is displayed by exceedingly low abundances of Fe, Mn and Co, whereas marked fluctuations in C/N_{atomic} ratios hint at the frequent occurrence of allogenic fluvial inputs into the playa system (Fig. 3). In addition, the (i) sand layer, (ii) reduced runoff input, and (iii) varved sediments altered to unvarved strata related to the Younger Dryas are also documented in the nearby lacustrine sequence of Ulaan Nuur in the Valley of Gobi Lakes (Fig. 1a; Lee et al. 2011), in the Lake Tana in northern Ethiopia (Lamb et al. 2007), and in the Lake Mondsee in Europe (Lauterbach et al. 2011), respectively. These features presumably characterize a benchmark lithofacies in the lacustrine sequences in the Gobi Desert of Mongolia or even on a larger northern hemispheric scale. In particular, this YD event-related Ca depletion with sharp boundaries of sand layer at c. 11 and 15 cal ka BP is also clearly recorded in the lacustrine core from Ulaan Nuur (Lee et al. 2011).

Unit V (< ~11 cal ka BP): lentic hypersaline lake with abruptly increased terrigenous inputs and authigenic productivity

An abrupt recovery of lacustrine conditions marks the termination of the late glacial stage as a chronological benchmark in the Orog Nuur catchment. This rapid increase of Ca abundance linked to the ameliorated Holocene climate is also recorded in Lake Mondsee in the northeastern Alps (Lauterbach et al. 2011). Likewise, the inception of Holocene is also marked by a sharp increase of pollen grains/concentration in the core ONW II (Murad 2011). The granulometric composition is akin to that of Units I and III with slightly higher clay and silt concentrations (Fig. 2; Al/Si ratio in Fig. 3). The most remarkable feature of the Holocene phase is the amount of hornblende and calcite corresponding to high Ca and $CaCO_3$ concentrations that are significantly greater relative to late Pleistocene units (Fig. 5). This feature suggests a considerably different hydro-geochemical habitat associated with paleoclimatic amelioration. The characteristic presence of carbonate indicates a predominant alkaline environment (higher Cl content) with abundant moisture supply and raised authigenic productivity (Wünnemann et al. 2010). This postulation is reinforced by the distinct assemblage of Ca in the biplot against Al/Si (Figs. 4b, 5; Norman and De Deckker 1990). Another reason for its occurrence, however, is that the calcite may also result from its recrystallization from detrital precursors (neogenic calcite; Pettijohn et al. 1973). In this case, more eroded clastic materials from the northern felsic and alkaline source terranes were brought into the Orog Nuur (Figs. 1b, 6). However, in terms of late Quaternary terrestrial (lacustrine) sediments, this diagenesis (recrystallization) may only have exerted limited influence on the bulk-geochemistry relative to the climate-induced calcite precipitation as well as allochthones input (Pettijohn et al. 1973; Yu et al. 2016). Furthermore, the significantly increased input of weathering materials is also demonstrated by the sharp increase of the Rb/Sr ratio (Fig. 3). In general, the higher Holocene lake level is in agreement with that from Lehmkuhl and Lang (2001). In the Baikal catchment further to the north (Fig. 1a), a wealth of palynological signals was assembled and assessed by Tarasov et al. (2007), who revealed a broadly warm and humid early Holocene as well as a deteriorated climate since the mid-Holocene. Nonetheless, in this study, due to the loss of the uppermost 24 cm of sediments and a relatively high uncertainty in the Holocene age in the Bayesian age model (Fig. 2), a feasible interpretation for the late Holocene signals is difficult to construct. Accordingly, the lentic hypersaline habit proposed here might be restrained to the early- to mid-Holocene period.

In summary, the distinct Holocene water body is attributed to (i) a more intensively weathered felsic/alkaline material transported from the higher catchment into the Orog Nuur depocenter, and (ii) sharply increased authigenic productivity of the alkaline environment thereafter (Fig. 6).

Conclusions

We present a continuous, high-resolution elemental record attained in the lacustrine sequence of Orog Nuur, southern Mongolia. An integrated paleoenvironmental and provenance history in the Gobi Desert that trace back to the MIS 3 are outlined for the first time.

To constrain the data quality, elements with high error margins relative to measured peak areas, and those elements/proxies under a significance level during the robust multivariate statistics are ruled out for further implications. As determined by robust multivariate statistics, the bulk-geochemistry of the Orog Nuur core sediments are governed by Factor 1 (grain-size composition), Factor 2 (authigenic productivity in the saline/evaporitic environment: Ca, Cl, $CaCO_3$, Factor 3 (allochthonous organic material input: TOC, C/N_{atomic}, and Factor 4 (fluvial terrigenous input, as well as quasi-constant aeolian input through the late Quaternary period: Al, Si, K, Ti, Fe, chlorite, and hornblende). As inferred from the biplot of Ca versus Al/Si, disparate source lithotypes along with authigenic productivity existed before and after Termination I. In contrast to the late Pleistocene, the Holocene was dominated by a distinctly high productivity alkaline environment due to the increased hydrodynamic strength of riverine inflow and intensified source rock weathering/erosion in the upper catchments of Orog Nuur. In order to gain a better understanding of the bulk geochemistry of lake sediments, the coupled provenance and environmental signatures, such as weathering and land surface processes in the catchment, need to be systematically discerned. Thus, considering the bulk-geochemistry of lacustrine sediments, paleoclimate would not be the sole governing factor; the coupled alteration of precursor rocks and accompanying decomposition/denudation intensity, as well as the transportation process may exert pivotal influences.

In the arid realm of Gobi Desert of Mongolia, two coarse sand layers corresponding to the LGM and Younger Dryas are present. In the Gobi Desert, these two layers provide a potential opportunity to act as chronological benchmarks. However, more investigation needs to be carried out to test the reliability of these beds on larger spatial scales and their synchrony in time.

Acknowledgements This study was funded by the German Research Foundation (LE 730/16-1), China Scholarship Council (201306190112), and National Natural Science Foundation of China (41701232). Fieldwork was supported by the Institute of Geography of the Mongolian Academy of Sciences (D Dorjgotov, A Tschimegsaichan). Radiocarbon dating was financed by a scholarship issued to W Murad. I Pipaud helped with the geologic mapping. F Schlütz and T Felauer supported the field work. We sincerely appreciate the constructive discussion with S Mischke, J Grunert, FH Chen, ACG Henderson, HY Lu, ZD Feng, JL Xiao, D Fleitmann, P Schulte, and I Obreht during the INQUA 2015 and EGU 2016. Editors TJ Whitmore, C Zhao, M Brenner, M Riedinger-Whitmore, and three anonymous reviewers are sincerely appreciated for improving the manuscript.

References

Baljinnyam I, Bayasgalan A, Brorisov BA, Cisternas A, Demyanovich MG, Ganbaatar L, Kochetkov VM, Kurushin RA, Molnar P, Philip H, Vashchilov YY (1993) Ruptures of major earthquakes and active deformation in Mongolia and its surroundings. Geol Soc Am Mem 181:26–52

Bertrand S, Hughen K, Giosan L (2015) Limited influence of sediment grain size on elemental XRF core scanner measurements. In: Croudace IW, Guy Rothwell R (eds) Micro-XRF studies of sediment cores. Developments in paleoenvironmental research, vol 17, pp 473–490

Boyle JF (2001) Inorganic geochemical methods in palaeolimnology. In: Last WM, Smol JP (eds) Tracking environmental change using lake sediments volume 2: physical and geochemical methods. Developments in paleoenvironmental research, vol 2, pp 83–130

Bridge JS, Demicco RV (2008) Earth surface processes, landforms and sediment deposits. Cambridge University Press, Cambridge, p 61

Calvert SE, Pedersen TF (2007) Elemental proxies for palaeoclimatic and palaeoceanographic variability in marine sediments: interpretation and application. In: Hillaire-Marcel C, De Vernal A (eds) Proxies in late cenozoic paleoceanography. Developments in marine geology, vol 1, pp 567–625

Chen FH, Yu ZC, Yang ML, Ito E, Wang SM, Madsen DB, Huang XZ, Zhao Y, Sato T, Birks HJB, Bommer I, Chen

JH, An CB, Wünnemann B (2008) Holocene moisture evolution in arid central Asia and its out-of phase relationship with Asian monsoon history. Quat Sci Rev 27:351–364

Chilingar GV, Zenger DH, Bissell HJ, Wolf KH (1979) Dolomites and dolomitization. In: Larsen G, Chilingar GV (eds) Diagenesis in sediments and sedimentary rocks. Developments in sedimentology, vol 25A, pp 428–536

Conroy JL, Overpeck JT, Cole JE, Liu KB, Wang L, Ducea MN (2013) Dust and temperature influences on glaciofluvial sediment deposition in southwestern Tibet during the last millennium. Glob Planet Change 107:132–144

Costa KM, Russel JM, Vogel H, Bijaksana S (2014) Hydrological connectivity and mixing of Lake Towuti, Indonesia in response to paleoclimatic changes over the last 60,000 years. Palaeogeogr Palaeoclimatol Palaeoecol 417:467–475

Cunningham WD (2005) Active intracontinental transpressional mountain building in the Mongolian Altai: defining a new class of orogeny. Earth Planet Sci Lett 240:436–444

Dapples EC (1979) Silica as an agent in diagenesis. In: Larsen G, Chilingar GV (eds) Diagenesis in sediments and sedimentary rocks. Developments in sedimentology, vol 25A, pp 99–142

Davies SJ, Lamb HF, Roberts SJ (2015) Micro-XRF core scanning in palaeolimnology: recent developments. In: Croudace IW, Guy Rothwell R (eds) Micro-XRF studies of sediment cores. Developments in paleoenvironmental research, vol 17, pp 189–226

Diekmann B, Hofmann J, Heinrich R, Fütterer DK, Röhl U, Wie KY (2008) Detrital sediment supply in the southern Okinawa Trough and its relation to sea-level and Kuroshio dynamics during the late Quaternary. Mar Geol 255:83–95

Dulski P, Brauer A, Mangili C (2015) Combined μ-XRF and microfacies techniques for lake sediment analyses. In: Croudace IW, Guy Rothwell R (eds) Micro-XRF studies of sediment cores. Developments in paleoenvironmental research, vol 17, pp 325–349

Felauer T (2011) Jungquartäre Landschafts und Klimagschichte der Südmongolei. Dissertation an der Fakultät für Georessourcen und Materialtechnik der RWTH Aachen. http://darwin.bth.rwth-aachen.de/opus3/volltexte/2011/3666/

Herzschuh U (2006) Palaeo-moisture evolution in monsoonal Central Asia during the last 50,000 years. Quat Sci Rev 25:163–178

Hunt JE, Croudace IW, MacLachland SE (2015) Use of calibrated ITRAX XRF data in determining turbidite geochemistry and provenance in Agadir Basin, Northwest African passive margin. In: Croudace IW, Guy Rothwell R (eds) Micro-XRF studies of sediment cores. Developments in paleoenvironmental research, vol 17, pp 127–146

Jarvis S, Croudace IW, Rothwell RG (2015) Parameter optimization for the ITRAX core Scanner. In: Croudace IW, Guy Rothwell R (eds) Micro-XRF studies of sediment cores. Developments in paleoenvironmental research, vol 17, pp 535–562

Johnsson MJ (1993) The system controlling the composition of clastic sediments. Geol Soc Am Spec Pap 284:1–20

Kazancı N, Gulbabazadeh T, Leroy SAG, Ataselim Z, Gürbüz A (2016) Aeolian control on the deposition of high altitude lacustrine basins in the Middle East: The case of Lake Neor, NW Iran. Quat Int. doi:10.1016/j.quaint.2015.11.040

Kylander ME, Ampel L, Wohlfarth B, Veres D (2011) High-resolution X-ray fluorescence core scanning analysis of Les Echets (France) sedimentary sequence: new insights from chemical proxies. J Quat Sci 26:109–117

Lamb H, Bates C, Coombes P, Marshall M, Umer M, Davies S, Dejen E (2007) Late Pleistocene desiccation of Lake Tana, source of the Blue Nile. Quat Sci Rev 26:287–299. doi:10.1016/j.quascirev.2006.11.020

Lauterbach S, Brauer A, Andersen N, Danielopol D, Dulski P, Hüls M, Milecka K, Namiotko T, Obremska M, Grafenstein U, Participants D (2011) Environmental responses to Lateglacial climatic fluctuations recorded in the sediments of pre-alpine Lake Mondsee (northeastern Alps). J Quat Sci 26:253–267

Lee MK, Lee YI, Lim HS, Lee JI, Choi JH, Yoon HI (2011) Comparison of radiocarbon and OSL dating methods for a late Quaternary sediment core from Lake Ulaan, Mongolia. J Paleolimnol 45:127–135

Lehmkuhl F, Lang A (2001) Geomorphological investigations and luminescence dating in the southern part of the Khangay and the Valley of the Gobi Lakes (Central Mongolia). J Quat Sci 16:69–87

Lehmkuhl F, Klinge M, Rother H, Hülle D (2016) Distribution and timing of Holocene and late Pleistocene glacier fluctuations in western Mongolia. Ann Glaciol 57:169–178

Leinen M (1989) The late Quaternary record of atmospheric transport to the northwest Pacific from Asia. In: Leinen M, Sarnthein M (eds) Paleoclimatology and paleometeorology: modern and past patterns of global atmospheric transport. Kluwer Academic Publishers, Dordrecht, pp 693–732

Martinez-Ruiz F, Kastner M, Gallego-Torres D, Rodrigo-Gámiz M, Nieto-Moreno V, Ortega-Huertas M (2015) Paleoclimate and paleoceanography over the past 20,000 years in the Mediterranean Sea Basins as indicated by sediment elemental proxies. Quat Sci Rev 107:25–46

Melles M, Brigham-Grette J, Minyuk PS, Nowaczyk NR, Wennrich V, DeConto RM, Anderson PM, Andreev AA, Coletti A, Cook TL, Haltia-Hovi E, Kukkonen M, Lozhkin AV, Rosén P, Tarasov P, Vogel H, Wagner B (2012) 2.8 million years of Arctic climate change from Lake El'gygytgyn, NE Russia. Science 337:315–320

Meyers PA, Lallier-Vergès E (1999) Lacustrine sedimentary organic matter records of late Quaternary paleoclimates. J Paleolimnol 21:345–372

Millot G (1970) Geology of clays, weathering, sedimentology, geochemistry. Springer, Vienna, pp 357–381

Mischke S, Herzschuh U, Zhang CJ, Bloemendal J, Riedel F (2005) A late Quaternary lake record from the Qilian Mountains (NW China): lake level and salinity changes inferred from sediment properties and ostracod assemblages. Glob Planet Change 46:337–359

Mischke S, Weynell M, Zhang CJ, Wiechert U (2013) Spatial variability of 14C reservoir effects in Tibetan Plateau lakes. Quat Int 313–314:147–155

Mukherji AK (1970) Analytical chemistry of zirconium and hafnium. Pergamon Press, Oxford, pp 1–11

Murad W (2011) Palynological studies on the late quaternary palaeoecology of the Gobi Desert in Mongolia. Ph.D. thesis, Georg-August-Universität Göttingen, p 128

Nesbitt HW, Young GM (1996) Petrogenesis of sediments in the absence of chemical weathering: effects of abrasion and sorting on bulk composition and mineralogy. Sedimentology 42:341–358

Nilson E, Lehmkuhl F (2001) Interpreting temporal patterns in the late Quaternary dust flux from Asia to the North Pacific. Quat Int 76(77):67–76

NIOZ, Avaatech (2007) XRF core scanner user manual version 2.0. Royal Netherlands Institute of Sea Research and Avaatech XRF Core Scanner Technology

Norman MD, De Deckker P (1990) Trace metals in lacustrine and marine sediments: a case study from the Gulf of Carpentaria, Northern Australia. Chem Geol 82:299–318

Ohlendorf C, Wennrich V, Enters D (2015) Experiences with XRF-scanning of long sediment records. In: Croudace IW, Guy Rothwell R (eds) Micro-XRF studies of sediment cores. Developments in paleoenvironmental research, vol 17, pp 351–372

Parnell AC, Haslett J, Allen JRM, Buck CE, Huntley B (2008) A flexible approach to assessing synchronicity of past events using Bayesian reconstructions of sedimentation history. Quat Sci Rev 27:1872–1885

Petschick R, Kuhn G, Gingele FX (1996) Clay mineral distribution in surface sediments of the South Atlantic: sources, transport, and relation to oceanography. Mar Geol 130:203–229

Pettijohn FJ, Potter PE, Siever R (1973) Sand and sandstone. Springer, New York, pp 24–63

Reimer PJ, Bard E, Bayliss A, Beck JW, Blackwell PG, Bronk Ramsey C, Grootes PM, Guilderson TP, Haflidason H, Hajdas I, HattŽ C, Heaton TJ, Hoffmann DL, Hogg AG, Hughen KA, Kaise KF, Kromer B, Manning SW, Niu M, Reimer RW, Richards DA, Scott EM, Southon JR, Staff RA, Turney CSM, van der Plicht J (2013) IntCal13 and Marine13 radiocarbon age calibration curves 0–50,000 years cal BP. Radiocarbon 55:1869–1887

Richter RO, van der Gaast S, Koster R, Vaars A, Gieles R, de Stigter HC, de Haas H, van Weering TCE (2006) The Avaatech XRF Core Scanner: technical description and applications to NE Atlantic sediments. In: Rothwell RG (ed) New techniques in sediment core analysis. Geological Society London Special Publications, vol 267, pp 39–50

Roser BP, Korsch RJ (1988) Provenance signatures of sandstone-mudstone suites determined using discriminant function analysis of major-element data. Chem Geol 67:119–139

Rother H, Lehmkuhl F, Fink D, Nottebaum V (2014) Surface exposure dating reveals MIS-3 glacial maximum in the Khangai Mountains of Mongolia. Quat Res 82:297–308

Scheffer F, Schachtschabel P (2002) Lehrbuch der Bodenkunde, 15th edn. Spektrum Akademischer Verlag, Berlin

Schillereff DN, Chiverrell RC, Croudace IW, Boyle JF (2015) An inter-comparison of μXRF scanning analytical methods for lake sediments. In: Croudace IW, Guy Rothwell R (eds) Micro-XRF studies of sediment cores. Developments in paleoenvironmental research, vol 17, pp 583–600

Schulte P, Lehmkuhl F, Steininger F, Loibl D, Lockot G, Protze J, Fischer P, Stauch G (2016) Influence of HCl pretreatment and organo-mineral complexes on laser diffraction measurement of loess–paleosol-sequences. CATENA 137:392–405

Shanahan TM, Overpeck JT, Hubeny JB, King J, Hu FS, Hughen K, Miller G, Black J (2008) Scanning micro-X-ray fluorescence elemental mapping: a new tool for the study of laminated sediment records. Geochem Geophys Geosyst 9:Q02016. doi:10.1029/2007GC001800

Sinha R, Smykatz-Kloss W, Stüben D, Harrison SP, Berner Z, Kramar U (2006) Late Quaternary paleoclimatic reconstruction from the lacustrine sediments of the Sambhar playa core, Thar Desert margin, India. Palaeogeogr Palaeoclimatol Palaeoecol 233:252–270

Stein R, Grobe H, Wahsner M (1994) Organic carbon, carbonate, and clay mineral distributions in eastern central Arctic Ocean surface sediments. Mar Geol 119:269–285

Stuiver MP, Reimer J, Bard E, Burr GS, Hughen KA, Kromer B, McCormac G, Jvd Plicht, Spurk M (1998) INTCAL98 radiocarbon age calibration. Radiocarbon 40:1041–1083

Tarasov PE, Bezrukova E, Karabanov E, Nakagawa T, Wagner M, Kulagina N, Letunova P, Abzaeva A, Granoszewski W, Riedel F (2007) Vegetation and climate dynamics during the Holocene and Eemian interglacials derived from Lake Baikal pollen records. Palaeogeogr Palaeoclimatol Palaeoecol 252:440–457

Tucker ME, Wright VP (1990) Carbonate sedimentology. Wiley, Oxford, pp 164–190

Vogt C (1997) Regional and temporal variations of mineral assemblages in Arctic Ocean sediments as climatic indicator during glacial/interglacial changes. Rep Polar Res 251:1–309

Weltje GJ, Tjallingii R (2008) Calibration of XRF core scanner for quantitative geochemical logging of sediment cores: theory and application. Earth Planet Sci Lett 274:423–438

Wirth SB, Gilli A, Niemann H, Dahl TW, Ravasi D, Sax N, Hamann Y, Peduzzi R, Peduzzi S, Tonolla M, Lehmann MF, Anselmetti FS (2013) Combining sedimentological, trace metal (Mn, Mo) and molecular evidence for reconstructing past water-column redox conditions: the example of meromictic Lake Cadagno (Swiss Alps). Geochim Cosmochim Acta 120:220–238

Wünnemann B, Demske D, Tarasov P, Kotlia BS, Reinhardt C, Bloemendal J, Diekmann B, Hartmann K, Krois J, Riedel F, Arya N (2010) Hydrological evolution during the last 15 kyr in the Tso Kar lake basin (Ladakh, India), derived from geomorphological, sedimentological and palynological records. Quat Sci Rev 29:1138–1155

Yang XP, Scuderi LA (2010) Hydrological and climatic changes in deserts of China since the late Pleistocene. Quat Res 73:1–9

Yu G, Cui F, Shi YF, Zheng Y (2007) Late marine isotope stage 3 paleoclimate for East Asia: a data-modal comparison. Palaeogeogr Palaeoclimatol Palaeoecol 250:167–183

Yu KF, Hartmann K, Nottebaum V, Stauch G, Lu HY, Zeeden C, Yi SW, Wünnemann B, Lehmkuhl F (2016) Discriminating sediment archives and sedimentary processes in the arid endorheic Ejina Basin, NW China using a robust geochemical approach. J Asian Earth Sci 119:128–144